Nanoscale

PAPER

View Article Online
View Journal | View Issue

Directional and enhanced spontaneous emission with a corrugated metal probe

Cite this: *Nanoscale*, 2014, **6**, 7512

Hongming Shen,[a] Guowei Lu,*[a] Yingbo He,[a] Yuqing Cheng,[a] Haitao Liu[b] and Qihuang Gong*[a]

A three-dimensional corrugated metal tapered probe with surface corrugated gratings at the tip apex is proposed and investigated theoretically, which leads to an obvious emission beaming effect of spontaneous emission from a single emitter near the probe. In contrast with conventional apertureless metal probes, where only the enhancement of an optical near-field is concerned, the corrugated probe is able to manipulate local excitation intensity and far-field emission direction simultaneously. The angular emission from a single dipole source, being placed close to the corrugated probe, falls into a cone with a maximum directivity angle of ±11.6°, which improves the collection efficiency 25-fold. Such a probe simultaneously increases the localized field intensity to about twice as strong as the conventional bare tip. In addition, the radiation pattern is sensitive to the working wavelength and the dipole to tip-apex separation. These findings make a promising route to the development of plasmonic spontaneous emission manipulation based on corrugated tapered antenna—for instance, tip-enhanced spectroscopy, single-molecule sensing, and single-photon source .

Received 25th February 2014
Accepted 30th April 2014

DOI: 10.1039/c4nr01037j

www.rsc.org/nanoscale

Introduction

The localized surface plasmon resonances (LSPRs) of nanostructures provide an ideal platform to manipulate photons at nanometer dimensions. One of the relevant applications is a simple tapered metal tip as an apertureless near-field probe, which is rapidly gaining in popularity because of its potential use in tip-enhanced Raman scattering (TERS),[1–4] chemical imaging,[5–8] light-emitting devices[9,10] and optical microscopy.[11–13] These applications usually benefit from strong electromagnetic fields concentrated at the tip apex due to LSPRs.[14] Up to now, a variety of optical probes, such as metal-coated tapered fibers,[15,16] single gold nanoparticles,[17] nanoparticle dimers or trimers,[18] so-called "bow-ties",[19] and metallic cones,[20–22] have been studied for enhancing photon emission rates from nearby single molecules or quantum dots. However, despite much progress, most of the previous efforts were concentrated on "superfocusing"[23] or near-field enhancement of the excitation process,[24] and less attention has been devoted to the modified directivity of light emission from the emitters near the optical probes.

The effect of optical antennas modifying the emission direction is well known. Modified directivities have been demonstrated, either theoretically or experimentally, in various kinds of nanostructures, including patch antennas,[25] nanowires,[26] compact nanodisk dimers,[27] or even single nanoparticles.[28–30] The approaches based on a gold nanoparticle coupled to a metallic tip have also been reported to obtain active angular control of emitted light.[31] Yet, a critical problem for dipolar optical emitters placed on a dielectric substrate is that the main beam directed into the substrate is largely confined around the critical angle, leading to poor directivity. For instance, Taminiau and colleagues demonstrated the control of the emission direction of individual molecules by reversible coupling to an optical monopole antenna.[32] Where the far-field emission is determined by the monopole antenna that behaves as an electronic dipole, the radiation directed mostly into the substrate spreads over a cone with peak maxima around the critical angle. In addition, Curto *et al.* observed unidirectional emission of individual quantum dots coupled to a Yagi–Uda antenna; however, the main beam is still highly concentrated around the critical angle.[33] In a more recent study, Lee *et al.* discovered that near-unity collection efficiency can be obtained by a planar dielectric antenna, whereas the emitted light falls into a cone with a sharp maximum near the critical angle so that a large numerical aperture objective is still required to capture most of the photons.[34] For optical measurements, especially in the tip-enhanced spectroscopy experiments, a high collection efficiency using a low numerical aperture objective is desirable and challenging. Although the topic of controlling emission direction has been investigated for various nanostructures, there is seldom a report on the beaming effect with a metal probe.

[a]*Department of Physics and State Key Laboratory for Mesoscopic Physics, Peking University, Beijing 100871, China. E-mail: guowei.lu@pku.edu.cn; qhgong@pku.edu.cn*

[b]*Key Laboratory of Optical Information Science and Technology, Ministry of Education, Institute of Modern Optics, Nankai University, Tianjin 300071, China*

Here we propose a three-dimensional (3D) metallic tapered probe with surface corrugated concentric grooves at the tip apex, acting as a directive antenna, to modify the angular radiation pattern of a single emitter. Fully vectorial simulation results show that such an antenna design offers a larger enhancement factor and more effective directional control in comparison with a conventional bare tapered tip. Remarkably, the corrugated probe can be engineered to achieve unparalleled narrow emission directivity to overcome the limit of the critical angle. Such nanostructures indicate a promising route to the development of a new type of tip-enhanced spontaneous-emission related technique, such as tip-enhanced fluorescence and Raman spectra, single-molecule sensing, single-photon source, highly efficient light-emission device, *etc.*

Methods

Fig. 1a illustrates the schematic of our proposed experimental arrangement based on a plasmonic corrugated apertureless probe. Ideally, radially polarized light at a wavelength of 633 nm is focused onto the tapered tip with a high-numerical-aperture objective lens. That will efficiently excite a *z*-oriented dipole emitter at an emission wavelength of 670 nm for the widely used Cyanine 5 dye molecule, for example. In our experiment, the emitter was placed at a distance of 10 nm upon the interface of two media with a refractive index ratio of 1.5 (*e.g.* glass/air). The enhanced radiation from such a dipole emitter is collected using the same objective lens. Fig. 1b shows the corrugated tip antenna design, which can be fabricated by current nanofabrication methods such as focused ion beam (FIB) milling and electrochemical etching.[24,35–38] In the calculations, the apertureless metallic tip is modeled as a gold conical taper with an opening angle of 30° terminated by a hemisphere with a radius of 10 nm. The dielectric function of gold is taken from ref. 39 and fitted by the Drude–Lorentz dispersion model. We optimize the structural parameters to obtain optimal directivity for the emission at a wavelength of ~670 nm. The groove period is 330 nm, with width 165 nm, depth 30 nm, and there are six grooves. In particular, the tip-end-to-first-groove distance is tailored to 630 nm for the best directivity performance. Due to the rotational symmetry of the structure, we performed 3D finite-difference time-domain (FDTD)[40] simulations in cylindrical coordinates. The perfectly matched layer (PML) absorption boundary is used and the mesh size is 2 nm in all cases (unless otherwise stated).

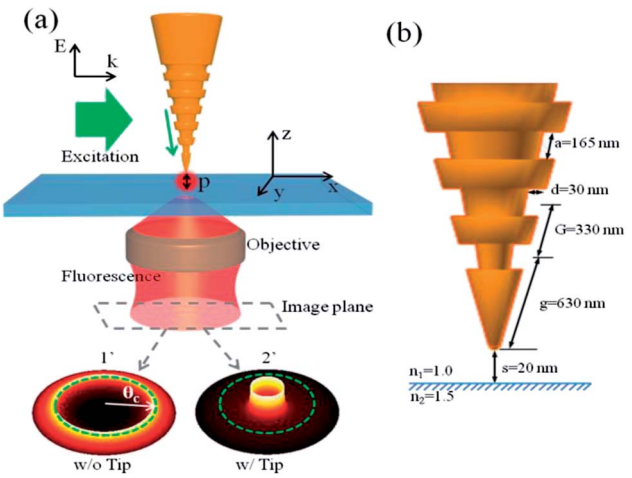

Fig. 1 (a) Schematics of the proposed experiment arrangement. The probe is illuminated by a focused, radially polarized beam. A *z*-oriented dipole source ($\lambda = 670$ nm) is placed at a distance of 10 nm upon the air/glass interface. 1′ and 2′ are dipole radiation pattern images without and with the tip antenna, respectively. The critical angle θ_c (green dashed line) is marked to show the beaming effect. (b) Side view and optimized structural sizes of the corrugated tip design. The conical tip-apex radius is 10 nm, with an opening angle of 30°. Groove period *G*, width *a*, depth *d*, and the tip-apex-to-first-groove distance *g* are set to be 330, 165, 30, and 630 nm, respectively.

Numerical simulations

(1) For the calculation of far-field radiation patterns, we recorded the near-field data [$\mathbf{E}(t)$, $\mathbf{H}(t)$] at a surface 100 nm beneath the air/glass interface by performing FDTD simulations in the cylindrical coordinates. In the calculations, the separation s between the tip and the substrate is 20 nm, and a *z*-oriented dipole emitter at a wavelength of 670 nm is placed in the middle. Although the near-to-far-field (NTFF) method is derived for a closed surface, here we chose one sufficiently large transformation surface (~14 μm wide) under the interface to capture most of the power directed to the substrate for a better approximation of the result, which has been successfully applied in the slit–groove structure.[42] Then we performed a Fourier transform to obtain the complex phasor field quantities ($\mathbf{E}$, $\mathbf{H}$) and calculated the surface electric (J_s) and magnetic (M_s) currents, respectively. According to the surface equivalence theorem, we calculated the time-averaged Poynting vector per unit solid angle, defined as:

$$\frac{\mathrm{d}P}{\mathrm{d}\Omega} = R^2\langle \mathbf{E}\times\mathbf{H}\rangle\hat{n} = \frac{k^2\eta}{32\pi^2}\left(\left|N_\theta + \frac{L_\phi}{\eta}\right|^2 + \left|N_\phi - \frac{L_\theta}{\eta}\right|^2\right),$$

where η is the impendence of the free space and k is the wave vector. More detailed information about the NTFF transformation can be found in Taflove's book.[41] Finally, we derived the angular directivity $D(\theta) = \pi P(\theta)/\int P(\theta)\mathrm{d}\theta$ for the lower half-space and collection efficiency $\kappa = P_{\mathrm{col}}/P_{\mathrm{em}}$ for our rotationally symmetric geometry. P_{col} is the collected power that enters an objective and P_{em} is the total power radiated to far-field from a single molecule.

(2) For the calculation of local field distribution, we performed a 3D FDTD simulation in the Cartesian coordinates. The structured tip is under side-illumination by a *z*-polarized plane wave at $\lambda = 633$ nm propagating along the *x* direction. In the 3D simulations, the mesh size is 5 nm to match memory resources and computation time.

(3) For the calculation of modified quantum efficiency and fluorescence enhancement, a temporal Gaussian point dipole source was implemented in the FDTD simulations, orienting in the *z* direction and referred to as a single Cy5 dye molecule. The Purcell factor $F = \Gamma_{\mathrm{rad}}/\Gamma^0_{\mathrm{rad}} = P_{\mathrm{rad}}/P^0_{\mathrm{rad}}$ and antenna efficiency $\eta_a = \Gamma_{\mathrm{rad}}/\Gamma_{\mathrm{tot}} = P_{\mathrm{rad}}/P_{\mathrm{tot}}$ can be obtained by calculating the

power radiated to the far-field P_{rad} (Poynting vector integrated over a closed surface that contains both the emitter and the tip) and the total power emitted by the dipole P_{tot} (Poynting vector integrated over a closed surface that only contains the emitter). The initial quantum efficiency of the Cy5 dye molecule in free solution is set to be 30%. To quantify the relative fluorescence enhancement, the excitation field enhancement at $\lambda = 633$ nm, modified quantum efficiency and collection efficiency at $\lambda = 670$ nm are considered together for comparison with an isolated dipole emitter on the substrate without any tip antenna.

Results and discussion

At first, the advantage of the plasmonic corrugated probe is demonstrated by comparing the far-field emission angular distribution of three cases, namely (a) an isolated free dipole emitter on the substrate without any tip antenna, (b) an emitter coupled to a bare tip, and (c) an emitter coupled to a corrugated probe. Fig. 2 shows the calculated far-field directivities in the x–z plane as a function of divergence angle, obtained with the near-to-far-field (NTFF) calculations.[41–43] For the rotational-symmetric geometry, the angular directivity is defined as $D(\theta) = \pi P(\theta)/\int P(\theta)\mathrm{d}\theta$, where $P(\theta)$ is the angular radiation power density and the integral is performed over the lower half space.[44] Fig. 2a depicts the typical radiation pattern of a single Hertzian dipole that is oriented perpendicular to the dielectric interface. We can see that the emission beam is directed into two lobes with a maximum directivity of $D \sim 3.1$ at an angle of $\pm 43.7°$, and this is in accordance with the emission pattern of a single electronic dipole. For a bare tip structure (Fig. 2b), the emission pattern has few changes, with a maximum directivity of $D \sim 3.5$ at $\pm 45.7°$ (slightly larger compared with the isolated free dipole). By introducing the surface concentric gratings (Fig. 2c), a remarkable change appears in that most of the radiation falls into a cone with a direction angle of $\pm 11.6°$, which is more than 30 degrees narrower than that of the isolated dipole and of the bare tip antenna. Specifically, its maximum directivity D is 6.5 with a full-width at half-maximum (FWHM) of $\sim 11°$, indicating that the corrugated tip not only can achieve light beaming, but also improves directivity compared with the other two cases. To quantify the ability of beaming light by the corrugated tip antenna, we define the factor $\kappa_1 = P_{col}/P_{down}$ as the ratio of the collected power that enters an objective with a maximum detectable angle of θ_m to the power directed into the bottom substrate. For a 1.2 N.A. water-immersion objective, corresponding to a maximum detectable angle of $\pm 64°$, the factors κ_1 of the three cases are: (a) 92.1%, (b) 93.5%, and (c) 99.2%, respectively. However, in the case of an objective with 0.5 N.A. (maximum detectable angle of $\pm 22°$), it is interesting to note that the factor κ_1 for the corrugated probe still reaches 82.3%—much higher than that of the isolated dipole (6.3%) and the bare tip (14.0%). This unique beaming effect has not been observed in previous studies and indicates promising routes for tip-enhanced spectroscopy measurements. Moreover, for a bare tip, we find that 59% of the light is emitted to the air and only a small percentage ($\sim$9%) is directed to the substrate. In the case of the corrugated tip, the light emitted to the air is about 28% and to the substrate is about 35%. Even so, for both cases more than 30% of the power is lost because of the metal. Finally, we obtain the collection efficiency, defined as $\kappa = P_{col}/P_{em}$, where P_{em} is the total power radiated to far-field from a single molecule. The simulation result indicates that the collection efficiency of the corrugated tip can achieve levels $\sim$25 times higher than that of the bare tip, corresponding to a 0.5 N.A. objective.

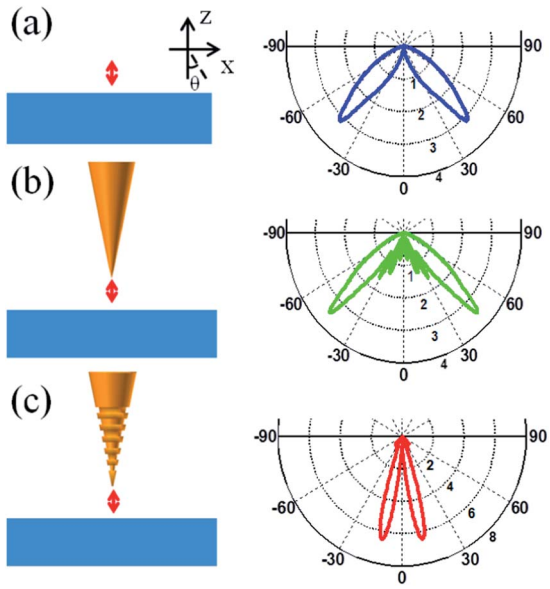

Fig. 2 Far-field radiation patterns in the x–z plane obtained with the NTFF method for three cases: (a) an isolated dipole emitter, (b) a dipole emitter coupled to a bare tip, and (c) a dipole emitter coupled to a corrugated tip with concentric gratings. Simulation results show that the radiated power of the emitter coupled to the corrugated tip is highly directed into the substrate, with the maximum directivity $D \sim 6.5$ at an angle of $\pm 11.6°$, improving the collection efficiency 25-fold compared with that of the bare tip.

We ascribe the beaming phenomenon to an interference effect between direct emission from dipole source and surface waves scattered by the grooves toward the far field. This mechanism is similar to the "bull's eyes" antenna,[45,46] although the antenna under consideration in this paper is more complicated because of its three-dimensional complex configuration. With Green's function formalism,[47] each scatterer of the subwavelength groove on the tip can be approximately considered as an effective point-like source (*i.e.* a circular line source with rotational symmetry) that radiates into free space. Thus, the total electric field radiated into the far-field at a polar angle θ can be expressed as,

$$\mathbf{E}_{tot}(\theta) = \mathbf{E}_0(\theta) + \mathbf{E}_1(\theta)e^{i\varphi_1} + \mathbf{E}_2(\theta)e^{i\varphi_2} + \ldots \quad (1)$$

where $\mathbf{E}_0$ represents the vectorial electric field directly radiated by the dipole emitter with the bare tip (without the scatterer of grooves), and $\mathbf{E}_i$ denotes the field radiated by the ith effective point source (which represents the field scattered by the ith groove) with an initial phase of φ_i. Since $\mathbf{E}_0$ for a bare tip has no beaming effect (see Fig. 2b), eqn (1) clearly shows that the beaming effect of $\mathbf{E}_{tot}$ should come from the interference

between $\mathbf{E}_0$ and the field $\mathbf{E}_i e^{i\varphi_i}$ scattered by the grooves. Generally $\mathbf{E}_i e^{i\varphi_i}$ should depend on all structural parameters (such as groove distances G and g, conical taper angle α, emission wavelength λ), and by tuning the structural parameters it is possible to achieve a constructive interference between $\mathbf{E}_0$ and $\mathbf{E}_i e^{i\varphi_i}$ at specific polar angles θ so as to obtain full directional control. For instance, in a weak scattering regime (such as for tiny grooves), the initial phase φ_i of the ith effective point source is approximately determined by the phase of the incident surface plasmon, which is efficiently excited by the z-polarized dipole emitter,[48] propagates along the unperturbed bare tip, and impinges at the ith groove. Then we have $\varphi_i = k_{sp}[g + (i-1)G]$ with k_{sp} being the propagation constant of the surface plasmon (actually, k_{sp} should depend on the cross-sectional radius of the bare tip, but here we assume k_{sp} to be constant at different positions on the tip surface for simplicity), and it is explicitly seen that φ_i is tunable simply by adjusting the groove distances G and g and wavelength λ (although note that k_{sp} also depends on λ). Our aim here is to provide general physical guidelines to understand the simulation results. A detailed rigorous model needs further effort beyond the scope of this paper.

Next we turn to the local field enhancement in the excitation process using 3D-FDTD calculations. In the calculation, a z-polarized plane wave at the wavelength of 633 nm is incident from the left side, as in the experiment, which can be achieved by focusing a radially polarized laser beam with a high N.A. objective lens. Fig. 3 demonstrates the time-averaged electric field intensity $|\mathbf{E}_z|^2$ (the z-component that is dominant over other components) around the tip end in the x–z plane for a probe without and with the gratings. We observe a high field confinement ("hot spot") at the tip-apex for both cases because of the excitation of LSPRs.[14] Fig. 3e shows the local excitation field enhancement $\eta_{exc} = |\mathbf{E}|^2/|\mathbf{E}_0|^2$ along the vertical line (a–a′), where $|\mathbf{E}_0|^2$ represents the incoming field intensity. It can be seen that the maximum field enhancement at the tip apex for the corrugated probe is twice as large as for the bare tip. The extra field enhancement is ascribed to the contribution of a grating-coupling effect of the surface plasmons. As is well known, the coupled photon to surface waves require the momentum conservation condition $k_{//} \pm qk_G = k_{sp}$, where $k_{//}$ is the parallel wave vector of far-field radiation, q an integer, $k_G = 2\pi/G$, with G the groove period and k_{sp} the in-plane propagation constant of the surface wave.[45] The grating here provides the necessary momentum matching, so as to enhance the coupling efficiency of surface plasmons coherently. It should be noted that a higher local field enhancement can be obtained through further optimally designing the groove parameters and tuning the angle of incidence.

It is worth discussing the performance of spatial resolution, which is a well-known feature of TERS, resulting from the highly localized field at the tip apex.[5] Fig. 3c and d present the field distribution in a plane parallel to the substrate and 5 nm under the tip apex for probes without and with gratings, respectively. Corresponding local excitation enhancements along line profile (b–b′) are shown in Fig. 3f. It can be seen that the highest enhancement occurs at the center for both cases. Moreover, we find the normalized curves of localized field enhancements

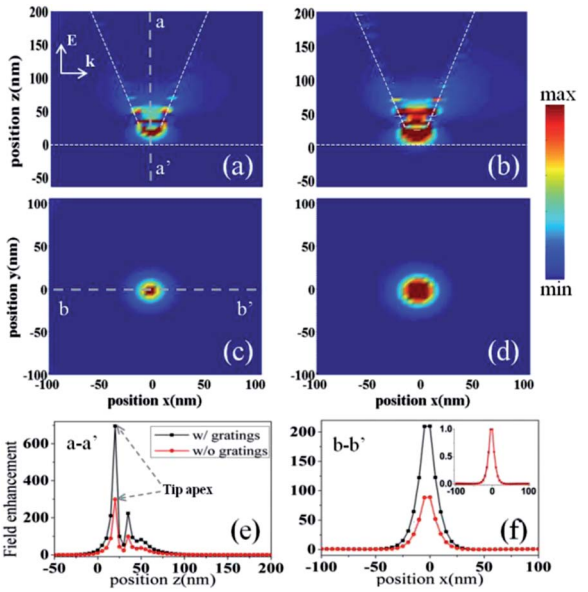

Fig. 3 3D FDTD simulations of electric field intensity $|\mathbf{E}_z|^2$ (the dominant z-component): (a) and (b) for tip without and with gratings in the x–z plane, (c) and (d) for tip without and with gratings in a plane parallel to the substrate and 5 nm under the tip apex. (e) and (f) demonstrate the local excitation enhancements along line profile a–a′ (along the tip axis) and b–b′. Specially, the inset in (f) is the corresponding normalized curves of localized field enhancement. It can be seen that the maximum field enhancement at the tip apex for the corrugated tip is 696-fold, more than twice that of the bare tip, but the spatial resolutions are almost the same for the two cases (~18 nm). The mesh grid here is set to be 5 nm. The polarization **E** and wave vector k of the incoming light are also sketched in (a).

(inset to Fig. 3f) are almost the same and the spatial resolution, defined as the FWHM of the local field enhancement, is ~18 nm for the two cases. Thus, an interesting result derived from our simulation is that the gratings have obvious influence on the local field enhancement, but almost no influence on the spatial resolution. The spatial resolution is mainly determined by the tip apex size.[14]

Now the modified spontaneous emission intensity by the corrugated probe is assessed systematically. As is well known, the general surface plasmonic enhanced fluorescence factor η_F can be expressed approximately as $\eta_F \propto \eta_{exc}\eta_\phi\eta_k$ under weak excitation,[46,49] with the local excitation enhancement $\eta_{exc} = |\mathbf{E}|^2/|\mathbf{E}_0|^2$, collection efficiency enhancement $\eta_k = \kappa/\kappa_0$, and quantum efficiency enhancement $\eta_\phi = \eta/\eta_0$. For an isolated emitter in free space, the quantum efficiency is $\eta_0 = \Gamma^0_{rad}/(\Gamma^0_{rad} + \Gamma^0_{nrad}) = \Gamma^0_{rad}/\Gamma^0_{tot}$, with radiative decay rate Γ^0_{rad} and nonradiative decay rate Γ^0_{nrad}. Due to the presence of a metallic nanostructure, the spontaneous emission rate of nearby single molecules would be changed and the modified quantum efficiency is given by

$\eta(\omega) = \eta_0(\omega)/\{[(1 - \eta_0(\omega))]/F(\omega) + \eta_0(\omega)/\eta_a(\omega)\}$,[50–52] where $F = \Gamma_{rad}/\Gamma^0_{rad} = P_{rad}/P^0_{rad}$ is the Purcell factor, and $\eta_a = \Gamma_{rad}/\Gamma_{tot} = P_{rad}/P_{tot}$ is the antenna efficiency. Here we assume the original quantum efficiency in free solution, η_0, to be 30% and an objective with 0.5 N.A. is used to collect the dipole emission at 670 nm. Table 1 summarizes the relative contributions from

excitation and emission gains to the total fluorescence enhancement effect at the emitter position. Note the enhancement factors are all normalized to an isolated dipole emitter on the substrate without any tip antenna. From the simulation results, we observe enormous fluorescence enhancement up to ~1660-fold for the corrugated tip, nearly 55 times higher than that of the bare tip. This remarkable enhancement factor is mainly due to the high directivity and also due to a minor contribution from the local excitation gain. The quantum efficiency enhancement is almost the same for the two cases. It is clearly indicated that the grating structure plays an important role in both efficient excitation and detection. In the excitation, the grating structure converts free propagating optical radiation to localized energy at the tip apex with an increase in excitation gain factor from 37 to 90. In the emission, the grating structure acts as a directive antenna to direct the far-field angular distribution of a single molecule, improving the collection efficiency nearly 25 times higher as compared with the bare tip for a low N.A. (0.5) objective.

Lastly, we demonstrate the dependence of the radiation pattern on the wavelength and separation distance. As shown in Fig. 4a–c, by changing the emission wavelength of a dipole emitter from 560 nm to 650 nm, a gradual decrease can be noted in the main direction angle, from 27° to 13°, while the trend is broken and the light pattern is split into two cones when wavelength further increases to 750 nm. According to eqn (1) and the related analysis, the emission wavelength will affect the phase relationship between the emission directly radiated from a single dipole (the first term) and the scattered field that is excited by the surface waves at the gratings (the following terms). Another parameter playing an important role in determining the radiation properties is the dipole-to-tip-apex separation d_1. Here the dipole source with wavelength 670 nm is fixed at a distance of 10 nm above the substrate, but the position of the tip apex varies, with $d_1 = 5$, 40, and 100 nm, respectively. From the simulation results of Fig. 4d–f, it can clearly be seen that the radiation is highly directed, with a narrow emission angle, when the dipole is placed very close to the tip apex ($d_1 < 30$ nm). With an increase in the separation d_1 further, more energy begins to radiate at the critical angle. This should result from a less efficient coupling from the dipole emitter to the surface waves on the probe,[48] which further weakens the field scattered by the gratings on the probe. This wavelength and separation dependence of the emission angular pattern provides a way for directional sorting of fluorescence emission from different molecule species in solution. Moreover, this method would lead to an increase of the signal-to-noise ratio during the tip-enhanced optical signal measurements, due to the difference in emission direction between the optimally enhanced signal and the unaffected background signal.

Our investigations also show that the parameter g plays an important role in controlling the fluorescence directivity. In addition, there is still much room to optimize antenna parameters for better performances. For instance, a higher plasmonic enhanced fluorescence intensity can be achieved by placing a corrugated tip close to a single nanoparticle (*e.g.* nanorod or nanosphere) to form a hybrid nanostructure. The nano-gap resonator will provide highly concentrated local plasmonic near-field due to the lightning rod effect,[14,21] and meanwhile the emission direction will be modified by the corrugated probe (data not shown here). It needs to be noted that the tip-apex-to-first-groove separation distance g of our proposed structure (~630 nm) is much smaller than that of the previously reported adiabatic tip (by more than 10 μm),[24] which is designed to separate the excitation area and the tip apex for low-background nanospectroscopy. Aperture–groove antennas made of a nano-aperture surrounded by periodic grooves milled in a thick gold film are a well-understood 2D planar structure.[46] For an intuitive understanding, the present metallic corrugated probe provides flexible 3D nanofocusing with a stronger local field enhancement than that of the planar nanostructures. Such 3D nanostructures can be designed to form an array for highly efficient light-emission devices. We believe that a narrower directionality of the emission pattern is possible with optimized structural parameters.

Table 1 Relative contributions from excitation and emission gains to the overall fluorescence enhancement

Nanostructures	η_{exc}	η_k	η_ϕ	η_F
Without gratings	37	0.4	2.3	30
With gratings	90	9	2.1	1660

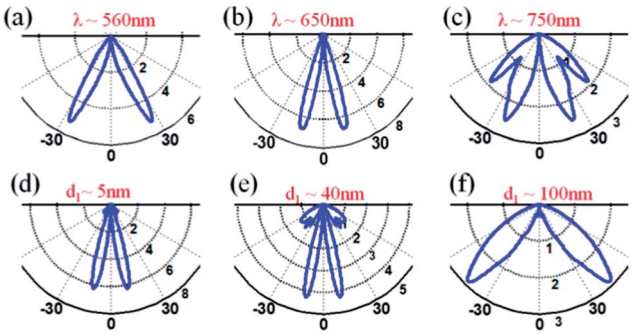

Fig. 4 Wavelength dependence of the radiation patterns: (a) $\lambda = 560$ nm, (b) $\lambda = 650$ nm, and (c) $\lambda = 750$ nm. For each wavelength, the emission can be directed along a certain direction, reflecting a complex interference phenomenon. (d)–(f) demonstrate the dependence of angular patterns on the dipole-to-tip-apex distance d_1, which takes values of 5, 40, and 100 nm, respectively. Note that the dipole source is fixed at a distance of 10 nm above the substrate, with an emission wavelength of 670 nm.

Conclusions

In summary, a 3D tapered metallic probe corrugated with several concentric gratings is proposed and exploited systematically. We calculate the angular radiation pattern, local field distribution, and quantum efficiency to quantify the excitation and emission gain to the overall spontaneous emission enhancement. The corrugated probe provides a powerful platform to tailor single-molecule emission intensity and far-field emission direction simultaneously, to give a high collection

efficiency. The simulation results show that the emission from a single oriented dipole coupled to the corrugated probe is highly directed into a cone with a narrow emission angle, and present a significant fluorescence enhancement factor. The enhancement factor is nearly 55 times higher than that of a bare tip, due to the high directivity and the contribution from the local excitation gain. Another remarkable point is the wavelength and separation dependence of the angular distribution pattern for spontaneous emission, which provides a way for directional sorting of the fluorescence and for increasing the signal-to-noise ratio. These findings make a promising route to the development of a corrugated-antenna-based spontaneous-emission manipulation for a wide range of novel applications, such as in analytical chemistry, light emission devices, and tip-enhanced fluorescence and Raman spectroscopy techniques.

Acknowledgements

This work was supported by the National Key Basic Research Program of China (grant no. 2013CB328703), the National Natural Science Foundation of China (grant nos 11374026, 91221304, 11121091, 61322508), and the Natural Science Foundation of Tianjin (grant no. 11JCZDJC15400).

Notes and references

1 B. Pettinger, P. Schambach, C. J. Villagómez and N. Scott, *Annu. Rev. Phys. Chem.*, 2012, **63**, 379–399.
2 N. Hayazawa, Y. Inouye, Z. Sekkat and S. Kawata, *Opt. Commun.*, 2000, **183**, 333–336.
3 H. Xu, E. J. Bjerneld, M. Käll and L. Börjesson, *Phys. Rev. Lett.*, 1999, **83**, 4357–4360.
4 M. D. Sonntag, J. M. Klingsporn, L. K. Garibay, J. M. Roberts, J. A. Dieringer, T. Seideman, K. A. Scheidt, L. Jensen, G. C. Schatz and R. P. Van Duyne, *J. Phys. Chem. C*, 2011, **116**, 478–483.
5 Y. Zhang, Z. C. Dong, S. Jiang, C. Zhang, L. G. Chen, L. Zhang, Y. Liao, J. Aizpurua, Y. Luo, J. L. Yang and J. G. Hou, *Nature*, 2013, **498**, 82–86.
6 F. De Angelis, G. Das, P. Candeloro, M. Patrini, M. Galli, A. Bek, M. Lazzarino, I. Maksymov, C. Liberale, L. C. Andreani and E. Di Fabrizio, *Nat. Nanotechnol.*, 2010, **5**, 67–72.
7 T. Ichimura, N. Hayazawa, M. Hashimoto, Y. Inouye and S. Kawata, *Phys. Rev. Lett.*, 2004, **92**, 220801.
8 M. Paulite, C. Blum, T. Schmid, L. Opilik, K. Eyer, G. C. Walker and R. Zenobi, *ACS Nano*, 2013, **7**, 911–920.
9 C. C. Neacsu, S. Berweger, R. L. Olmon, L. V. Saraf, C. Ropers and M. B. Raschke, *Nano Lett.*, 2010, **10**, 592–596.
10 S. Schmidt, B. Piglosiewicz, D. Sadiq, J. Shirdel, J. S. Lee, P. Vasa, N. Park, D. Kim and C. Lienau, *ACS Nano*, 2012, **6**, 6040–6048.
11 L. Novotny and S. J. Stranick, *Annu. Rev. Phys. Chem.*, 2006, **57**, 303–331.
12 B. Knoll and F. Keilmann, *Nature*, 1999, **399**, 134–137.
13 M. Fleischer, A. Weber-Bargioni, M. V. P. Altoe, A. M. Schwartzberg, P. J. Schuck, S. Cabrini and D. P. Kern, *ACS Nano*, 2011, **5**, 2570–2579.
14 Z. Yang, J. Aizpurua and H. Xu, *J. Raman Spectrosc.*, 2009, **40**, 1343–1348.
15 T. J. Antosiewicz and T. Szoplik, *Opt. Express*, 2007, **15**, 10920–10928.
16 Y. Wang, W. Srituravanich, C. Sun and X. Zhang, *Nano Lett.*, 2008, **8**, 3041–3045.
17 T. Kalkbrenner, M. Ramstein, J. Mlynek and V. Sandoghdar, *J. Microsc.*, 2001, **202**, 72–76.
18 C. Höppener, Z. J. Lapin, P. Bharadwaj and L. Novotny, *Phys. Rev. Lett.*, 2012, **109**, 17402.
19 J. N. Farahani, D. W. Pohl, H. J. Eisler and B. Hecht, *Phys. Rev. Lett.*, 2005, **95**, 17402.
20 S. Berweger, J. M. Atkin, R. L. Olmon and M. B. Raschke, *J. Phys. Chem. Lett.*, 2010, **1**, 3427–3432.
21 D. Sadiq, J. Shirdel, J. S. Lee, E. Selishcheva, N. Park and C. Lienau, *Nano Lett.*, 2011, **11**, 1609–1613.
22 S. Berweger, J. M. Atkin, R. L. Olmon and M. B. Raschke, *J. Phys. Chem. Lett.*, 2012, **3**, 945–952.
23 F. I. Baida and A. Belkhir, *Plasmonics*, 2009, **4**, 51–59.
24 C. Ropers, C. C. Neacsu, T. Elsaesser, M. Albrecht, M. B. Raschke and C. Lienau, *Nano Lett.*, 2007, **7**, 2784–2788.
25 R. Esteban, T. V. Teperik and J. J. Greffet, *Phys. Rev. Lett.*, 2010, **104**, 26802.
26 T. Shegai, V. D. Miljkovic, K. Bao, H. Xu, P. Nordlander, P. Johansson and M. Käll, *Nano Lett.*, 2011, **11**, 706.
27 T. Pakizeh and M. Käll, *Nano Lett.*, 2009, **9**, 2343.
28 G. Pellegrini, P. Mazzoldi and G. Mattei, *J. Phys. Chem. C*, 2012, **116**, 21536.
29 D. Vercruysse, Y. Sonnefraud, N. Verellen, F. B. Fuchs, G. Di Martino, L. Lagae, V. V. Moshchalkov, S. A. Maier and P. Van Dorpe, *Nano Lett.*, 2013, **13**, 3843.
30 I. M. Hancu, A. G. Curto, M. Castro-López, M. Kuttge and N. F. van Hulst, *Nano Lett.*, 2013, **14**, 166.
31 E. Le Moal, S. Marguet, B. Rogez, S. Mukherjee, P. Dos Santos, E. Boer-Duchemin, G. Comtet and G. Dujardin, *Nano Lett.*, 2013, **13**, 4198.
32 T. H. Taminiau, F. D. Stefani, F. B. Segerink and N. F. Van Hulst, *Nat. Photonics*, 2008, **2**, 234–237.
33 A. G. Curto, G. Volpe, T. H. Taminiau, M. P. Kreuzer, R. Quidant and N. F. van Hulst, *Science*, 2010, **329**, 930–933.
34 K. G. Lee, X. W. Chen, H. Eghlidi, P. Kukura, R. Lettow, A. Renn, V. Sandoghdar and S. Gotzinger, *Nat. Photonics*, 2011, **5**, 166–169.
35 B. Ren, G. Picardi and B. Pettinger, *Rev. Sci. Instrum.*, 2004, **75**, 837–841.
36 P. Nagpal, N. C. Lindquist, S. Oh and D. J. Norris, *Science*, 2009, **325**, 594–597.
37 N. C. Lindquist, P. Nagpal, A. Lesuffleur, D. J. Norris and S. H. Oh, *Nano Lett.*, 2010, **10**, 1369–1373.
38 S. S. Kharintsev, G. G. Hoffmann, A. I. Fishman and M. K. Salakhov, *J. Phys. D: Appl. Phys.*, 2013, **46**, 145501.
39 P. B. Johnson and R. W. Christy, *Phys. Rev. B: Condens. Matter Mater. Phys.*, 1972, **6**, 4370–4379.

40 A. F. Oskooi, D. Roundy, M. Ibanescu, P. Bermel, J. D. Joannopoulos and S. G. Johnson, *Comput. Phys. Commun.*, 2010, **181**, 687–702.
41 A. Taflove and S. C. Hagness, *ComputationalElectrodynamics: The Finite-Difference Time-Domain Method*, Artech House, Norwood, MA, 3rd edn, 2005.
42 Y. C. Jun, K. C. Y. Huang and M. L. Brongersma, *Nat. Commun.*, 2011, **2**, 283.
43 S. Kim, S. Kim and Y. Lee, *Phys. Rev. B: Condens. Matter Mater. Phys.*, 2006, **73**, 235117.
44 P. Bharadwaj, B. Deutsch and L. Novotny, *Adv. Opt. Photonics*, 2009, **1**, 438.
45 H. Aouani, O. Mahboub, E. Devaux, H. Rigneault, T. W. Ebbesen and J. Wenger, *Nano Lett.*, 2011, **11**, 2400–2406.
46 H. Aouani, O. Mahboub, N. Bonod, E. Devaux, E. Popov, H. Rigneault, T. W. Ebbesen and J. Wenger, *Nano Lett.*, 2011, **11**, 637–644.
47 A. B. Evlyukhin, G. Brucoli, L. Martín-Moreno, S. I. Bozhevolnyi and F. J. García-Vidal, *Phys. Rev. B: Condens. Matter Mater. Phys.*, 2007, **76**, 075426.
48 D. E. Chang, A. S. Sørensen, P. R. Hemmer and M. D. Lukin, *Phys. Rev. Lett.*, 2006, **97**, 053002.
49 M. J. Levene, J. Korlach, S. W. Turner, M. Foquet, H. G. Craighead and W. W. Webb, *Science*, 2003, **299**, 682–686.
50 A. Kinkhabwala, Z. Yu, S. Fan, Y. Avlasevich, K. Mullen and W. E. Moerner, *Nat. Photonics*, 2009, **3**, 654–657.
51 A. Mohammadi, F. Kaminski, V. Sandoghdar and M. Agio, *J. Phys. Chem. C*, 2010, **114**, 7372–7377.
52 A. Pascal, B. Palash and N. Lukas, *Phys. Rev. Lett.*, 2006, **96**, 113002.